Analysis and Decoupling of Multisource EMI in High-Power PV Inverter

Yi Yu, Xuejun Pei, *Senior Member, IEEE*, Peng Zhou, Qichi Chen, and Dingkun Zhao

***Abstract*—The photovoltaic (PV) inverter contains four types of converters, the active neutral point clamped (ANPC) inverter, the boost converter, the ac auxiliary (ACAUX) flyback converter, and the dc auxiliary (DCAUX) flyback converter. The coupling of single-source electromagnetic interference (EMI) generated by these different converters forms multisource EMI. The contributions of each single-source EMI are hidden in the coupled multisource EMI. Therefore, the modeling and suppression may not be highly targeted. In this article, the decoupling method of multisource EMI in high-power PV inverter is investigated. First, the studied PV inverter and its multisource EMI are analyzed. Second, the LF multisource EMI is decoupled based on the discrete spectrum. Third, the HF multisource EMI is decoupled based on the time–frequency matrix. Finally, the proposed decoupling method is implemented to both LF and HF EMI of a 100 kW PV inverter. The targeted suppression strategies are adopted based on the decoupled single-source EMI. The peak EMI spectra dominated by DCAUX, ACAUX, and ANPC are decreased by 18, 10, and 7 dB, respectively. The results validate the correctness of the proposed decoupling method.**

***Index Terms*—Discrete spectrum, dominant EMI source, multisource EMI decoupling, photovoltaic (PV) inverter, time–frequency matrix.**

Nomenclature

HF	High-frequency band above 5 MHz.
LF	Low-frequency band between 150 kHz and 5 MHz.
LISN	Line impedance stabilization networks.
QP	Quasi-peak.
RBW	Resolution bandwidth.
CE	Conducted emission.
RE	Radiated emission.
STFT	Short-time Fourier transform.
X_t^f	Element of the time–frequency matrix at time t and frequency f.
F	Frequency index of the time–frequency matrix.
FR	Frequency resolution.
T	Time index of the time–frequency matrix.
TR	Time resolution.
G	Window function.
M	Window width.
L	Window overlap length.
R	Window step size.

Manuscript received 20 January 2024; revised 19 March 2024 and 10 May 2024; accepted 2 June 2024. Date of publication 19 June 2024; date of current version 4 September 2024. This work was supported by the National Natural Science Foundation of China under Grant 52377187 and Grant 51977091. Recommended for publication by Associate Editor C. K. Tse. *(Corresponding author: Xuejun Pei.)*

The authors are with the School of Electrical and Electronic Engineering, Huazhong University of Science and Technology, Hubei, Wuhan 430070, China, and also with the Power Electronics and Energy Management Key Laboratory, Ministry of Education of China, Wuhan 430070, China (e-mail: d202180645@hust.edu.cn; ppei215@mail.hust.edu.cn; zhou_p@hust.edu.cn; M202171930@hust.edu.cn; m202171898@hust.edu.cn).

Color versions of one or more figures in this article are available at https://doi.org/10.1109/TPEL.2024.3416693.

Digital Object Identifier 10.1109/TPEL.2024.3416693

I. Introduction

THE EMI emitted by photovoltaic (PV) inverters shortens the life of power components and reduces the reliability of PV power generation systems [1], [2], e.g., reduces the health of the power transformer [3]. Moreover, wide-bandgap semiconductor devices are widely used [4], which further exacerbates EMI emissions. Commercial PV inverters must pass electromagnetic compatibility (EMC) standards [5] before they are promoted to the market. Because of the large size components and the already established layout structure, EMI optimization in high-power converters is time-consuming, labor-intensive, and extremely restrictive, and even requires a redesign from scratch. Accurate analysis of the EMI emission mechanism can help debug and suppress EMI, which has attracted widespread attention in recent years [6], [7].

Although the study of EMI for a single converter is quite mature [8], [9], not enough attention has been paid to the study of EMI in multiconverter systems. PV inverters, as typical multiconverter systems with multiple EMI sources coupled, bring new challenges to the analysis of the EMI mechanism. The multisource EMI needs to be decoupled into single-source EMI so that the mature method for single-source EMI can be adopted. Besides, dominant EMI sources can be identified based on the decoupled EMI. With unknown dominant sources, high-power EMI filters may be over-designed, which significantly increases the cost and volume. Only by decoupling the multisource EMI can prediction, model correction, and overall EMI suppression be more precisely completed. Therefore, research on multisource EMI decoupling is urgently needed.

To decouple the multisource EMI, some measurement methods can be used [10], [11], [12], [13]. These methods require multichannel or multicondition measurements. The multichannel measurement method uses the same oscilloscope to simultaneously measure the standard EMI and the EMI sources within the converter [10], [11]. However, this method is limited by the number of oscilloscope channels and measurement convenience. The multicondition measurement method decouples the multisource EMI based on changes in system parameters such as starting and stopping one by one. However, there is a problem with the interaction mechanism between converters [13]. System EMI is significantly different from that of just a single converter

TABLE I
COMPARISONS OF DIFFERENT DECOUPLING AND IDENTIFICATION METHODS

Method	Ref	Accuracy	Cost	Complexity	With QP/AV Detection	Applicable for CE and RE	Applicable Converters
Discrete spectrum for LF EMI Time–frequency matrix for HF EMI	This article	**Perfect**	**Low**	**Low**	**Yes**	**Both**	**Various power and voltage levels**
Multichannel measurement	[10],[11], 2020	**Perfect**	High	Moderate	No	Only CE	Not for high-power converters
Multicondition measurement	[12],[13], 2020	Good	Moderate	Moderate	No	Only CE	Not for control-coupled converters
MFA	[14],[15], 2023	Moderate	Moderate	Moderate	No	Only RE	Not for high-switching-frequency converters
Blind source separation	[16],[17], 2023	Good	Moderate	High	No	Only RE	**Various power and voltage levels**
Basic emission waveform theory	[18],[19], 2022	Good	High	High	No	**Both**	Not for large-size converters
Empirical mode decomposition	[20],[21],[22], 2018	Poor	High	High	No	Only RE	**Various power and voltage levels**
Artificial intelligence	[23],[24], 2023	Unpredictable	High	High	No	**Both**	Only for converters with database

operating independently, which may cause identification errors. Therefore, the measurement methods are difficult to be applied to compact high-power converters.

As an alternative, postprocessing-based decoupling methods are more attractive [14], [15], [16], [17], [18], [19], [20], [21], [22], [23], [24]. These methods rely on advanced signal processing. Multisource EMI signals obtained from single-channel measurements are separated according to specific characteristics. The method named modulation frequency analysis (MFA) is proposed in [14] and [15]. Based on the modulation frequency graph, the switching frequency of the EMI sources can be determined, which helps to identify the noise source. However, MFA cannot be used to rank the noise sources because periodic signals are highlighted in this method. The blind source separation method is applied to decouple multi-source EMI in [16], [17]. A specified clustering algorithm is introduced to deal with the time domain EMI. The accuracy is good but the calculation time is long. Therefore, the method is not suitable for real-time processing. A novel interpretation and source identification method named basic emission theory is proposed and verified in [18] and [19]. This innovation theory characterizes emission with four basic waveforms, including square wave, sine wave, damped oscillation, and spike wave. Although the method is generalized for electronic systems, specialized complex fitting algorithms are required. The well-known empirical mode decomposition (EMD) has been widely used in EMI processing [20], [21], [22]. Complex EMI signals are decomposed into several intrinsic modal functions (IMFs). While the IMFs cannot provide enough accuracy for the decoupling. As the general method, artificial intelligence is also applied to decoupling multisource EMI [23], [24]. No prior information is needed for the method, but machine learning needs a big database. The accuracy is also unpredictable, and the cost is extremely high. As a summary, the comparison of the above-mentioned methods is given in Table I, which shows the existing methods all have their limitations in accuracy, cost, and applicability. However, the method proposed in this article offers better accuracy, lower cost, and reduced complexity. In addition, it is applicable to both CE and RE, complying with EMC standards for specified QP and average (AV) detection. Since the proposed method only relies on known modulation strategies and time-domain EMI measurement under standard configurations, this method is applicable to power converters with various power and voltage levels.

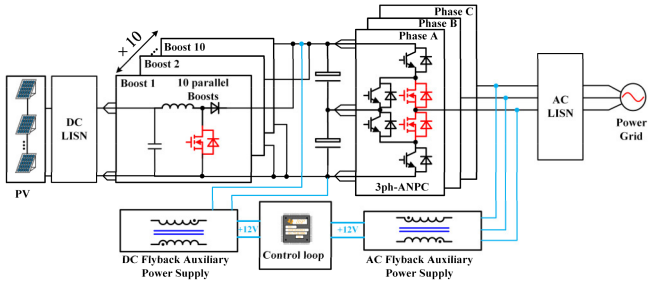

Fig. 1. 100 kW PV inverter with AC and DC LISNs.

In this article, the analysis and decoupling of multisource EMI for a 100-kW PV inverter are studied. The proposed decoupling method can reveal the true single-source EMI spectrum from multisource EMI. With the help of the decoupled single-source EMI, dominant EMI sources can be identified, and targeted suppression can be adopted. Section II analyzes the multi-source EMI in the studied PV inverter. In Section III, the decoupling method of LF multisource EMI is proposed. In Section IV, the time–frequency matrix is introduced to decouple the HF EMI. In Section V, the proposed decoupling method is implemented to both LF and HF EMI of a prototype PV inverter. The targeted suppression strategies are adopted based on the decoupled single-source EMI, the results of which validate the correctness of the proposed decoupling method. Finally, Section VI concludes this article.

II. ANALYSIS OF THE MULTISOURCE EMI

Fig. 1 shows the schematic diagram of a 100-kW PV inverter with ac and dc LISNs. The PV inverter consists of four types of power electronic converters: the three-phase three-level active neutral point clamped (ANPC) inverter, 10 parallel boost converters for maximum power point tracking, dc auxiliary (DCAUX) and ac auxiliary (ACAUX) flyback power supplies. Table II shows the modulation strategies of each converter. The two auxiliary power supplies are both needed by the control loop for various working situations. The boost converters increase the dc voltage from the PV panel. The ANPC inverts the dc voltage into three-phase ac power and feeds it into the grid. The AC LISN is installed between the PV inverter and the grid. The DC LISN is installed between the PV inverter and the PV panel. The

TABLE II
MODULATION STRATEGIES OF FOUR CONVERTERS IN PV INVERTER

Converter	Modulation Strategies
ANPC	Discontinuous PWM with fixed 20 kHz
Boost	PWM with fixed 18 kHz
ACAUX	Quasi-resonant zero-voltage-switching PWM with variable frequency around 80 kHz
DCAUX	Quasi-resonant zero-voltage-switching PWM with variable frequency around 90 kHz

measured EMI by the LISNs should comply with the specified limits in [5].

The switching devices in red shown in Fig. 1 are SiC MOSFET devices. The black devices are Si IGBT devices. The working frequencies of the Si devices in ANPC are much slower than those of SiC devices. Compared to Si switching devices, SiC has fast switching transients and small switching loss, which makes it very suitable for high-efficiency high-power converters. Because of faster-switching transients, SiC devices have stronger HF EMI compared to Si [25].

Every switching device in every converter leads to the voltage and current pulse. Thus, the broadband EMI is produced in the switching transients. The EMI generated by each converter propagates to every part of the PV inverter. Thus, the EMI is coupled to each other, resulting in multisource EMI. The contributions of each single-source EMI are hidden in the coupled multisource EMI. Therefore, the dominant EMI source is hard to determine. The decoupling of multisource EMI is urgently needed for prediction and targeted suppression.

The LF EMI has a discrete spectrum due to the PWM modulation. The fixed or near-fixed switching frequencies result in discrete spikes in the spectrum. However, the HF EMI abovementioned approximately 5 MHz has a continuous spectrum not the same as LF EMI, which is due to the switching frequency fluctuations. The actual digital controller cannot fully guarantee the ideal perfect fixed switching frequency, which means that there must be fluctuations in the switching frequency. The frequency fluctuations lead to spread spectrum spikes with a certain width. The width of the spectrum spikes at higher frequencies is larger, as a result, the spikes are connected and the continuous spectrum is formed. Taking boost EMI as an example, even if the frequency fluctuation of the 18 kHz switching frequency is only 1 ‰ (18 Hz), at HF EMI above 5 MHz, the frequency fluctuation will be expanded to 278 times (5 kHz). The width of the spread spectrum spikes is much larger. Therefore, the spectrum spikes become difficult to distinguish. The other modulation strategies like DPWM and variable frequency PWM even have a much larger spike width, which leads to more undistinguishable spectra. After the coupling of EMI sources, multisource HF EMI is completely continuous without discrete spikes.

Due to the different spectrum, the LF and HF multisource EMI are decoupled based on two corresponding parts of the proposed method. The LF and HF multisource EMI are all measured in the standard-specified setup, except for using an oscilloscope instead of an EMI receiver to measure EMI. The LF EMI is decoupled based on the discrete spectrum with the help of known modulation strategies. The HF EMI is decoupled based on the

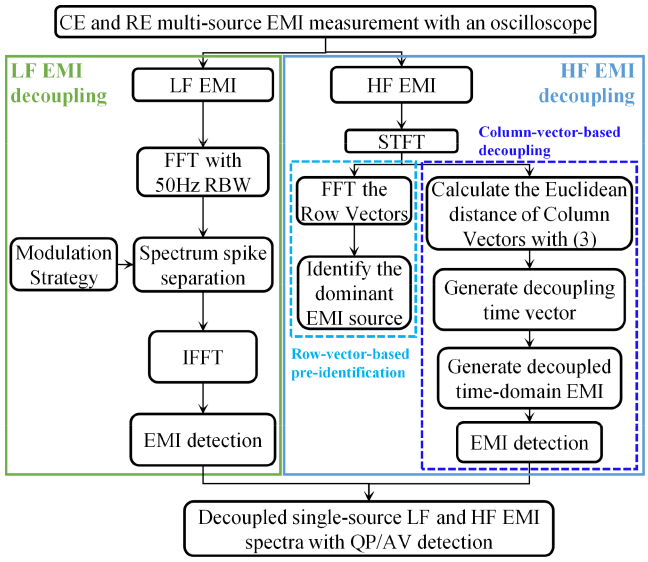

Fig. 2. Guideline of multisource EMI decoupling.

time–frequency matrix derived from STFT. Row-vector-based dominant source preidentification is suitable for rapid analysis at the testing site due to the simplest process. Besides, the column-vector-based decoupling can acquire accurate magnitudes of each single-source EMI considering QP/AV detection for further targeted modeling and suppression. The decoupling guideline is summarized as a flowchart in Fig. 2, which is gradually illustrated in the following sections.

III. DECOUPLING OF LF MULTISOURCE EMI BASED ON DISCRETE SPECTRUM

A. Detailed Spectrum of LF EMI

RBWs specified in the standard are 9 kHz for CE and 120 kHz for RE. This setup takes into account the tradeoff between spectral resolution accuracy and measurement speed. The bigger the RBW, the faster the measurement speed, but the worse the spectral resolution.

The RBW specified in the standard cannot provide enough spectrum details to decouple the multisource EMI. Fig. 3 also compares the spectrum with standard RBW measured by an EMI receiver and the spectrum with 50 Hz RBW measured by an oscilloscope. The two EMI are both sensed by AC LISN. Due to the principle of step sweep in the EMI receiver, the fine 50 Hz RBW measurement setting results in an excessively long time. The FFT-based time domain measurement is conducted on the oscilloscope. The measurement time is 20 ms, which means 50 Hz RBW. The sampling frequency is 500 MHz. Fig. 3 shows that more spectral details are obtained for the 50 Hz RBW, allowing different EMI spikes to be separated, thus decoupling LF multisource EMI.

B. LF Multisource EMI Decoupling Method Based on the Discrete Spectrum

The discrete spectral spikes play a critical role in decoupling the LF multisource EMI. Studies have confirmed that PWM

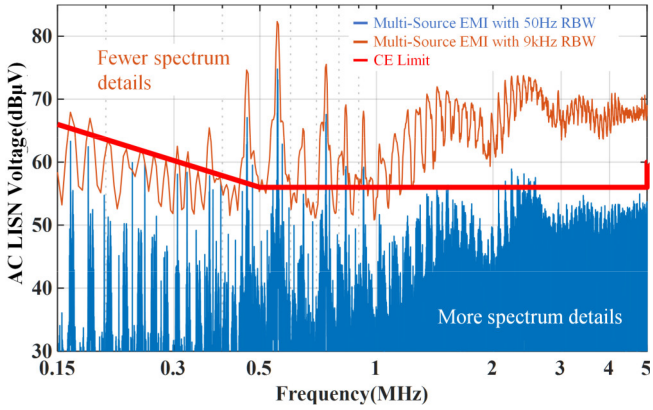

Fig. 3. AC LISN spectrum comparison between the standard RBW of 9 kHz and the narrower RBW of 50 Hz.

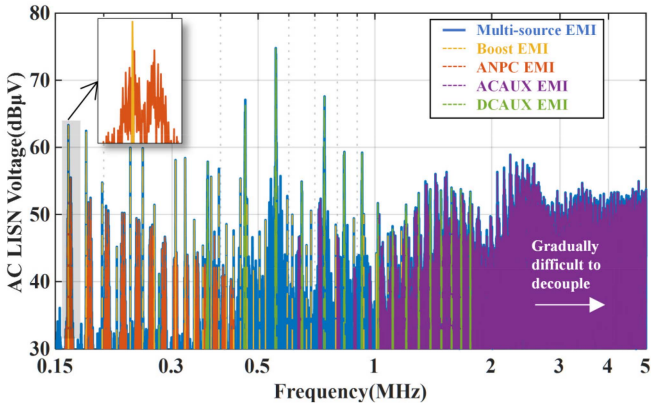

Fig. 4. Predecoupled LF multisource EMI without QP/AV detection.

converters emit spectral spikes corresponding to multiples of their switching frequencies [26]. Moreover, different modulation strategies have different spectra even if the switching frequency is the same. Within the LF multisource EMI, distinct switching frequency multiples are identifiable and are represented in various colors in Fig. 4. Specifically, four types of frequency multiples are present, 18, 20, 81.2, and 92.6 kHz, exactly corresponding to the switching frequencies of different converters in Table II. By separating the EMI spikes with different types of switching frequency multiples in the spectrum, multisource EMI can be predecoupled into single-source EMI without QP/AV detection.

Despite the frequency band overlap between the ANPC and boost spikes, it is still possible to separate the two spectra. The enlarged area of Fig. 4 illustrates the spectrum of the ANPC overlapping the boost near 160 kHz. The single spike at 162 kHz ($= 18\,\text{kHz} \times 9$) is excited by the boost converter, while the spread spikes with a certain width are excited by ANPC. This is because the ANPC adopts a sinusoidal modulation of the DPWM with sideband harmonics. Therefore, the 50 Hz RBW spectra provide enough details to distinguish the EMI generated by converters with different modulations.

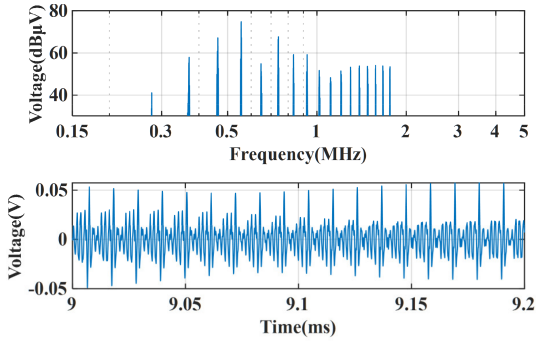

Fig. 5. Frequency and time domain waveform of the pre-decoupled DCAUX EMI.

However, the QP/AV detection results specified in the standard require unique RBW and detector charge/discharge factors [5]. The predecoupled spectrum results without QP/AV detection cannot directly compare with the standard limit. Therefore, further processing is needed for decoupling LF EMI. The separated single-source EMI spectra need to be transformed back into the time domain waveform, which can be fed into the QP and AV detection algorithms proposed in [27] that mimic EMI receivers. Taking the spectrum of DCAUX as an example, Fig. 5 shows both the frequency and time domain waveform of the predecoupled DCAUX LF EMI. Other EMI spectrum components that are not excited by the DCAUX are set to zero. The rest spectrum is then converted back into a time-domain single-source EMI waveform by IFFT, only after which single-source EMI can be detected for QP and AV results.

These detected results can be directly compared with the standard limits for certification, which avoids misjudgment of dominant EMI sources without QP/AV detection. For example, in the enlarged area of Fig. 4, boost has a higher undetected EMI spectrum than ANPC. However, ANPC has a larger spike width than boost. The sideband harmonics of the ANPC accumulate with each other in the QP/AV detected spectrum [28], producing even higher EMI than boost. The final decoupled and detected LF EMI QP results are displayed in Section V. Therefore, ANPC is the true dominant EMI source in this band, which means the undetected spectrum may lead to wrong dominant sources.

The LF EMI decoupling part in Fig. 2 shows the procedures of how the LF EMI is decoupled. The multisource EMI is measured by LISN in a standard test configuration. The time-domain EMI is then sampled by an oscilloscope with the sampling frequency set to 500 MHz and the sampling time to 20 ms. The sampled time-domain EMI is imported into MATLAB to compute the FFT spectrum at 50 Hz RBW. The different classes of single-source spikes in the LF EMI spectrum up to 5 MHz are distinguished. The multisource EMI is separated into different single-source spectra. Next, the single-source EMI is subjected to the IFFT operation to obtain predecoupled single-source time-domain EMI. These time-domain EMI are fed into the MATLAB program of the simulated EMI receiver [27] to calculate the QP and AV results. Finally, the detected spectra of different single-source EMI are spliced together to form the decoupled LF EMI output.

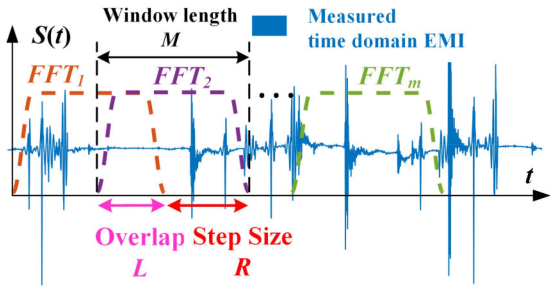

Fig. 6. Principles of STFT.

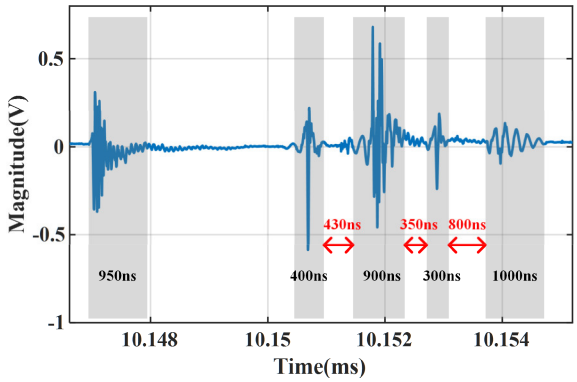

Fig. 7. Analysis of the multisource EMI time domain waveform for determining STFT parameters.

IV. Decoupling of HF Multisource EMI Based on Time–Frequency Matrix

The HF multisource EMI has a continuous spectrum and cannot be decoupled through spectrum information alone. Therefore, this part introduces the theory of time–frequency analysis to overcome the limitation that FFT only focuses on the frequency domain. The elements of the time–frequency matrix contain both time and frequency domain information. From the perspective of time–frequency matrix row vectors, the dominant EMI source can be quickly identified. From the perspective of time–frequency matrix column vectors, the multisource EMI can be decoupled.

A. Time–Frequency Matrix of the HF EMI

The short-time Fourier transform (STFT) and wavelet transform (WT) are the two most widely used time–frequency analysis algorithms [29], [30]. The more complex WT has multiresolution ability, which STFT does not have. WT can deal with broadband signals. Note that the decoupling problem only needs to be for HF EMI, and the decoupling problem for LF EMI can be solved by analyzing the spectral spike intervals as shown in Section III. The disadvantages of STFT not being able to deal well with both HF and LF EMI do not appear, so the simpler STFT algorithm is chosen.

1) Principles of STFT: Fig. 6 shows the basic principles of STFT [29]. Analysis windows ($\boldsymbol{FFT}_1/\boldsymbol{FFT}_2/\boldsymbol{FFT}_{\mathrm{m}}$) of length M are applied to different moments of the measured time-domain EMI. The step size between adjacent analysis windows is R and the width of the window overlap is L. The FFT results are the spectral vectors at the center time of the window. The calculated vectors for the different windows form the time–frequency matrix of the STFT. The window function tapers at the edges to improve time domain truncation and avoid false ringing caused by spectral leakage. A nonzero window overlap length of L is usually specified, as the overlap compensates for signal attenuation at the edges of the window. The specific expression for STFT given in (1) is modified from [29], where X_t^f is the spectral component of the signal at the time number t and frequency number f, g is the window function, FR is the frequency resolution and N is the total number of points of the input time domain signal. R is the step size of the window function.

The output X_t^f of (1) is the elements of the time–frequency matrix at row f and column t. $g(n-t\times R)$ and $\mathrm{e}^{-j2\pi n(f\text{-}1)\cdot FR}$ can be thought of as time and frequency selector items. The former selects the component at the moment $t\times R$ in the input EMI $x(n)$, and the latter selects the component of the frequency $(f\text{-}1)\cdot FR$ in the input EMI $x(n)$. By calculating X_f^t for different combinations of f and t, the time–frequency matrix can be obtained. The time–frequency matrix is the most important tool for decoupling HF multisource EMI in this article

$$X_t^f = \sum_{n=1}^{N} x(n)g(n - t \times R)e^{-j2\pi n(f-1)\cdot FR}. \tag{1}$$

2) Determining the Key Parameters of the Time–Frequency Analysis: The window function is determined first. The Hanning window is chosen because it has both good FR and less spectral leakage [31]. To avoid missing the spikes due to the attenuated edge, an overlap of 75% is usually used. Therefore, $L = 0.75M$, $R = 0.25M$, and TR $= 0.25M/f_s$. f_s stands for sampling frequency.

Then, the window width M is determined. M should not be too large to distinguish between different spikes, nor too small for the STFT window to contain all the oscillations of a spike. Fig. 7 shows the time domain waveform of the signal to be decoupled. The different spike oscillations come from different EMI sources. The oscillation durations are emphasized by shadings. It can be seen that 1000 ns is sufficient to ensure that the STFT window contains the entire spike waveform. When the sampling frequency is 500 MHz, 1000 ns corresponds to a window size M of 500 pts. TR is now 125pts (250 ns). The spike interval in Fig. 7 is greater than 250 ns, which can realize the separation of different spikes. The rare case where two spikes overlap is analyzed in Section IV-C.

Finally, the FR is determined according to (2). After window length M is determined to be 500, the intrinsic FR' is locked to 1 MHz, but it does not provide enough spectral details for EMI at 5 MHz. Adding zeros to the end of the window before the Fourier transform helps to optimize FR. 500 zeros are added to the end of time-domain data within the window function, resulting in a total of 1000 pts, i.e., Zeros $=$ 500, corresponding to FR of

TABLE III
PARAMETERS OF STFT

f_s	FR	TR	M	L	R
500 MHz	0.5 MHz	250 ns	500 pts	375 pts	125 pts

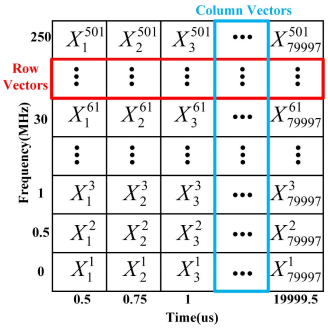

Fig. 8. Time–frequency matrix for multisource EMI.

0.5 MHz. This results in a smoother spectrum

$$FR' = \frac{f_s}{M} = \frac{500\,\text{MHz}}{500} = 1\,\text{MHz}$$
$$\Rightarrow FR = \frac{f_s}{M + \text{Zeros}} = \frac{500\,\text{MHz}}{500 + 500} = 0.5\,\text{MHz}. \quad (2)$$

The determined parameters of STFT are shown in Table III. The time domain EMI waveform with a sampling time of 20 ms and a sampling frequency of 500 MHz is subjected to STFT with these parameters according to (1). Fig. 8 shows the derived 501 × 79 997 time–frequency matrix. Each row element of the matrix has the same frequency and different times, and each column element has the same time and different frequencies. The time interval between windows is 0.25 μs. The values of the matrix elements are complexes at different frequencies and times. It is noted that only the amplitudes are used in the matrix. For both CE and RE test cases, a time–frequency matrix is generated for each. The red-marked row vectors and the blue-marked column vectors in Fig. 8 are used to decouple multisource EMI.

The time–frequency graph is the most important form of representation of the STFT results. It does not work well when dealing with the decoupling of four EMI sources. By color-coding the amplitude of the time–frequency matrix in Fig. 8, a time–frequency graph of HF CE EMI from 5 to 30 MHz can be obtained as shown in Fig. 9. By analyzing the dominant EMI time–frequency interval, specifically the interval marked in red with a high magnitude in Fig. 9, the switching frequency of the dominant EMI source can be determined. As can be seen in Fig. 9, at 6–7 MHz, 6–8 ms is dominated by ACAUX of around 80 kHz switching frequency. However, in the same frequency range, in the time range of 16–17 ms, EMI from multiple sources has almost the same amplitude and the dominant EMI source is difficult to determine.

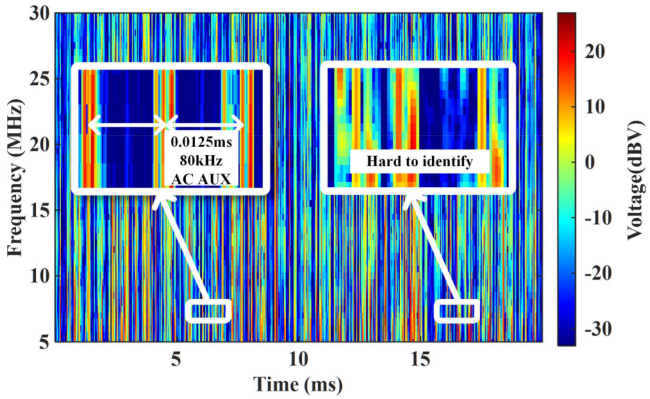

Fig. 9. Limitations of using the time–frequency graph for CE HF EMI decoupling.

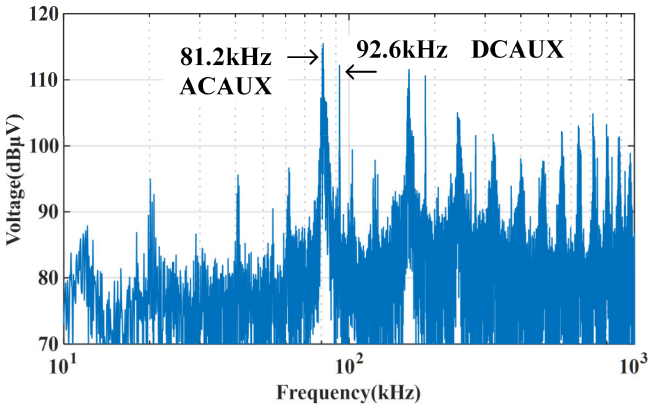

Fig. 10. Identification results for the dominant EMI source at 7 MHz based on the spectrum of the 15th-row vector.

B. *Identification of HF Dominant EMI Sources Based on Time–Frequency Matrix Row Vectors*

Applying FFT to the row vectors of the time–frequency matrix helps to address the challenge of distinguishing features within the time–frequency graph. The process of time–frequency graph identification essentially involves, for each frequency band, locating equidistant intervals of high-magnitude regions, often indicated by a redder color. Alternatively stated, the equivalent goal is to search for periodic patterns within each row of the time–frequency matrix, which can be efficiently identified using FFT.

Taking the example of finding the dominant EMI sources at 7 MHz, which corresponds to row 15 of the time–frequency matrix, the spectrum of this row vector is calculated. Since the total number of points is 79 997 and the sampling time is 20 ms, the sampling frequency at present is approximately 4 MHz. The spectrum result is shown in Fig. 10. It can be seen that the dominant EMI source in the row vector corresponding to 7 MHz is ACAUX with a switching frequency of 81 kHz. DCAUX with a switching frequency of 92 kHz has a slightly lower EMI. This is more accurate and efficient than the time–frequency graph-based identification.

Each row vector of the time–frequency matrix in Fig. 8 is FFT transformed to obtain 501 spectrums, extracting the maximum spike of each spectrum and the corresponding switching frequency to achieve fast and accurate identification of the dominant EMI sources in the full frequency band. The flowchart is shown in the row-vector-based quick preidentification part of Fig. 2.

Although the above-mentioned methods achieve dominant EMI source identification, they do not provide the exact spectral amplitude of single source EMI. In addition, the EMC standard tests require CE QP/AV results and RE QP results, both of which only the identification method cannot provide. Therefore, a more powerful decoupling method is needed.

C. Decoupling of HF Multisource EMI Based on Time–Frequency Matrix Column Vectors

The essence of decoupling multiple EMI sources is the grouping of time domain spikes. The same group contains only the time domain spikes generated by the switching of a particular EMI source. Subsequently, QP/average detection is performed on each group of time-domain spikes to obtain full-band EMI detection results for every source. These results can then be directly compared against the prescribed EMC standard limits.

Note that the EMI time domain spikes generated by different EMI sources have a unique spectral signature due to the different propagation paths and the different amplitudes of the EMI sources themselves. This signature is embedded in the column vector of the time–frequency matrix.

For the boost, ACAUX, and DCAUX, the EMI spikes emitted by the same EMI source at different moments are similar, whereas those from different sources are not. Therefore, the multisource EMI can be decoupled based on the similarity of the spikes.

The column vector characterizes the spectrum of the EMI spikes at different times. Spikes with similar column vectors are grouped. The degree of similarity between two vectors can be determined using Euclidean distance. The smaller the Euclidean distance, the more similar the two column vectors are and the more likely to be emitted from the same EMI source. Equation (3) shows the grouped discriminant function for the CE HF EMI column vector, which quantifies the similarity of different column vectors and is also the defining formula for the Euclidean distance. Rows 11–61 of the time–frequency matrix correspond to HF CE frequencies from 5 to 30 MHz. The Euclidean distance d_{ij} between each column vector X_i^n and the reference column vector X_j^n in the time–frequency matrix is solved. Radiated EMI is consistent with this form. Comparison of the Euclidean distance d of the column vectors with the threshold value allows similar time-domain EMI spikes to be grouped. It should be noted that due to the difference in the rise and fall time of the switching pulse, the same source EMI is divided into two groups of rising and falling spikes. These two sets of spikes are superimposed to give a complete single-source EMI

$$d_{ij} = \sqrt{\sum_{n=11}^{61} \left(\text{abs}(X_i^n) - \text{abs}(X_j^n)\right)^2}. \tag{3}$$

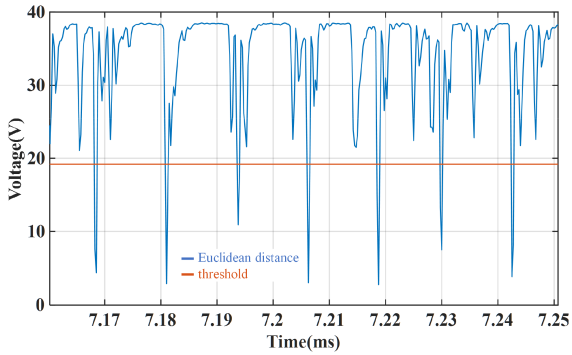

Fig. 11. Euclidean distance and the threshold for decoupling the column vectors.

The reference vector is selected based on the location of the time domain spike. The EMI spike at 10.1507 ms in Fig. 7 is chosen as an example to be decoupled. This time corresponds to column 40 602 of the time–frequency matrix. The Euclidean distance results for each column vector to the column 40 602 reference vector are shown in Fig. 11. The column vectors emitted by the same EMI source have a small Euclidean distance, with high similarity, but not the same, because the window function of STFT does not always align exactly with the time-domain EMI spike when it slides, and some spikes are affected by the attenuation of the edge of the window function. However, the Euclidean distances of column vectors in the same group are still quite different from those of other source column vectors.

The Euclidean distance threshold is chosen as half of the distance between the reference vector and the no-EMI column vector, resulting in a threshold of 19.2 as shown in Fig. 11. Each column vector is considered to originate from the same EMI source as the reference vector when their Euclidean distance is less than this threshold. Besides the interval of about 0.0125 ms (80 kHz) indicates that the row vector group belongs to ACAUX. Decoupling of the ACAUX EMI can be achieved by retaining the column vector times that meet the threshold and clearing the EMI spikes at other times. The spike retention range can be based on the width of the selected spike to improve resolution accuracy.

The spike width at 10.1507 ms is approximately 400 ns and a spike retention width of 500 ns can be selected, corresponding to 250 sampling points. This process can be achieved by multiplying the decoupling time vector shown in Fig. 12 with the original time domain EMI signal. The decoupling time vector keeps 1 when d is lower than the threshold, else keeping 0. The decoupled EMI time domain spikes shown in Fig. 13 are generated. It should be noted that an EMI source has two types of spikes, rising and falling, which need to be decoupled separately, the decoupled spike in the figure is generated by the falling edge of ACAUX.

There are two EMI spikes in the interval shown in the red box in Fig. 13. This is because the two EMI sources have almost identical switching moments and the time domain interval of the spikes is less than TR of the time–frequency matrix and cannot be separated.

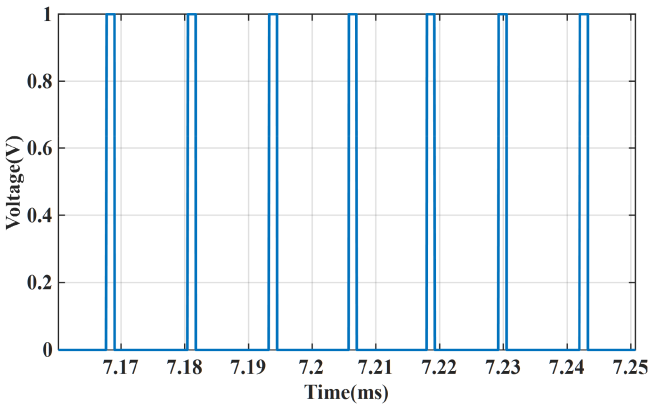

Fig. 12. Derived decoupling time vector after Euclidean distance thresholding.

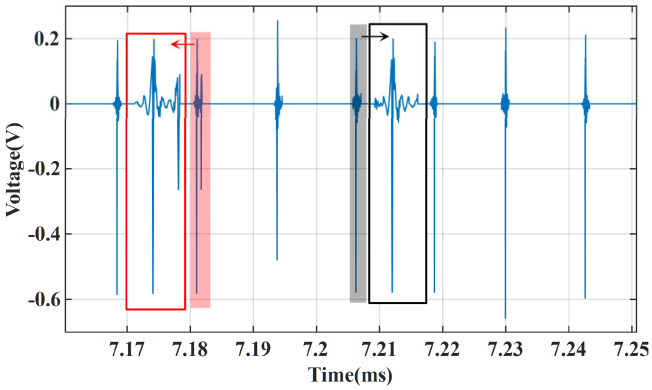

Fig. 13. Decoupled time-domain EMI spikes from ACAUX sources (falling edge only).

When EMI spikes overlap, these spikes are categorized into groups with more similar spectral peaks. The subtraction of column vector magnitudes in (3) uses linear magnitudes rather than logarithmic decibel magnitudes. This means that the similarity of the peak spectra is the dominant factor in determining the Euclidean distance. EMI spikes that are more similar at the peak have smaller Euclidean distances.

The above-mentioned process is repeated for six sets of different reference column vectors from three types of dc/dc EMI sources, and the rest is EMI excited by ANPC. Then, the decoupling of all EMI sources is realized, the flowchart of which is summarized in the column-vector-based decoupling part in Fig. 2.

The HF and LF decoupling methods proposed in this article are applicable to higher switching frequencies. For LF EMI decoupling up to 5 MHz, higher switching frequencies produce more easily distinguishable discrete spectra. Therefore, the LF decoupling method is not limited by higher switching frequencies. For HF EMI decoupling above 5 MHz, the maximum switching frequency that the method works well is limited by the width of the 1-μs window in the STFT. Therefore, the maximum applicable switching frequency is 1 MHz. It should be noted that for high-power PV inverters, the switching frequency is only kHz, which is significantly below 1 MHz. This ensures

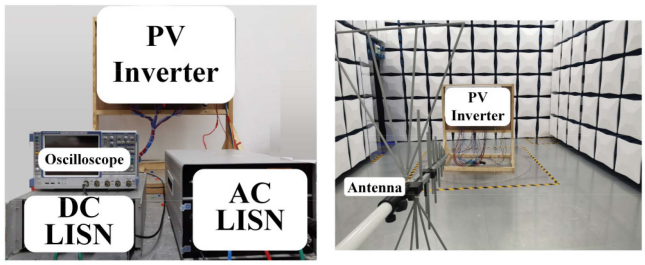

(a) (b)

Fig. 14. EMI test platform for the 100-kW PV inverter. (a) CE test platform. (b) RE test platform.

TABLE IV
PARAMETERS OF THE STUDIED PV INVERTER

Parameters	Value
DC Input Voltage	540 V
DC BUS Voltage	700 V
AC Grid Voltage/Frequency	380 V/50 Hz
Rated power	100 kW

the broad applicability of the proposed methods. Although the dc AUX source operates at approximately 90 kHz, both the LF and HF EMI can still be decoupled using methods proposed in this article, demonstrating their effectiveness for high switching frequencies even up to nearly 100 kHz.

V. EXPERIMENTAL VERIFICATION

A. Experimental Platform

Multisource EMI experimental platforms are shown in Fig. 14. Parameters of the studied PV inverter are shown in Table IV. CE and RE EMI are sensed by LISN and antenna. Then the transformed EMI voltages are measured by an oscilloscope R&S RTE 1024. This article analyzes the decoupling of CE EMI at the ac port and RE EMI for the whole PV inverter. The sampling frequency of the oscilloscope is set to 500 MHz and the number of sampling points is 10 M. Limited to the oscilloscope bandwidth, the radiated EMI is only analyzed to 200 MHz.

The results in the following experiments and the literature [33] also show that the EMI exceeding the standard limits is concentrated before 200 MHz. This is because high-power converters have low switching frequencies, which is due to the switching loss and heat dissipation. For the studied 100 kW PV inverter, all converters have switching frequencies less than 100 kHz. For the Y-inverter in [33], the switching frequency is 100 kHz, and the radiated EMI is concentrated before 140 MHz. The low switching frequencies make the HF radiated band greater than 200 MHz almost immune from radiated EMI.

B. Validation of LF Multisource EMI Decoupling

Fig. 15 shows the decoupling results of LF EMI based on the discrete spectrum. The LF multisource and the decoupled single-source EMI are all detected for QP results [27]. AV results are similar and therefore are not shown. The dominant EMI sources are identified based on the decoupled EMI. Then, the

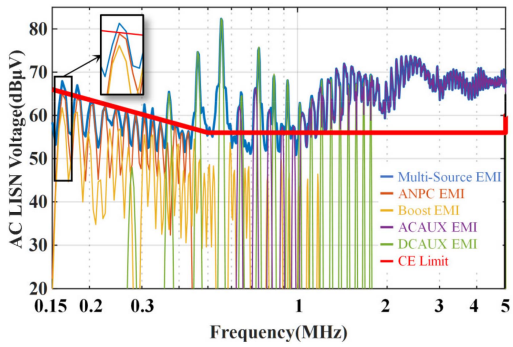

Fig. 15. QP spectrum comparison of the LF multisource EMI with decoupled single-source EMI.

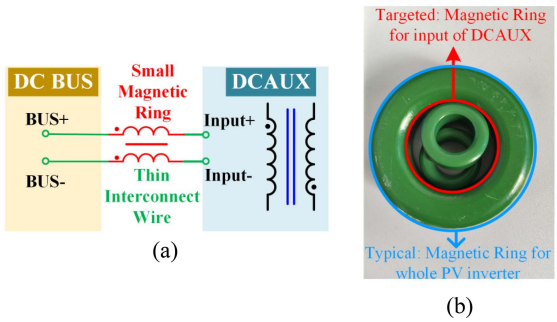

Fig. 16. Targeted suppression for LF multisource EMI. (a) Schematic. (b) Size comparison between targeted and typical suppression.

TABLE V
IDENTIFICATION RESULTS OF DOMINANT EMI SOURCES

	Frequency (MHz)				
	6.5	13	25	35	80
Dominant Source	ACAUX	ANPC	ANPC	ANPC	ACAUX

TABLE VI
PARAMETERS OF THE TARGETED SUPPRESSION STRATEGIES

Target sources	Components	Detail parameters
LF DCAUX	small magnetic ring	Permeability 7000 Dimensions 25×15×10 mm
HF ACAUX	*Y* capacitor	4.7 nF
HF ACAUX	damping resistor	1 Ω
HF ANPC	buffer capacitor	1.5 nF

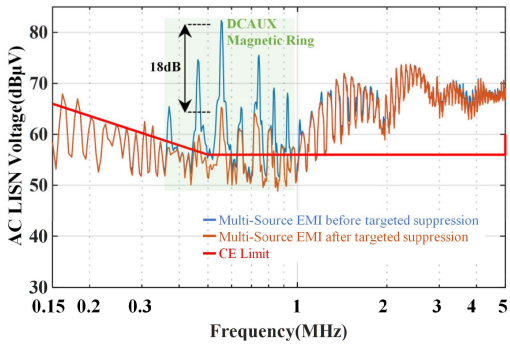

Fig. 17. QP spectrum comparison of the LF multisource EMI before and after targeted suppression.

targeted LF EMI suppression is developed to verify the accuracy of the LF decoupling method.

First, the comparison between Figs. 4 and 15 illustrates the importance of simulating EMI receiver processing. In the frequency band around 160 kHz, boost EMI is greater than ANPC in the 50 Hz RBW spectrum of Fig. 3. However, in the 9 kHz RBW spectrum after the detector operation, the EMI magnitudes of boost and ANPC are comparable in Fig. 15, which proves the superiority of the proposed decoupling method. The possible changes of the dominant EMI source under different RBW are fully considered. The 9 kHz RBW specified in the standard should be adopted.

Then, the LF dominant EMI sources are analyzed based on the decoupled EMI. As shown in Fig. 15, the peak LF EMI frequency is 560 kHz. At this frequency, the DCAUX is the dominant source of LF EMI with the highest magnitudes and should be targeted for suppression measures. The main propagation path of the DCAUX is through the dc BUS and then through the *N* line or ANPC circuit output to the ac LISN in Fig. 1. The measured multisource EMI is dominated by common mode (CM) EMI. Therefore, the targeted suppression strategies exclusively address CM EMI.

Fig. 16 illustrates the targeted suppression strategy for the DCAUX. A small magnetic ring is installed on the input cable of the DCAUX, plotted in red in Fig. 16. Typical suppression strategies require that the ring be installed at the ac output of the PV inverter, where the cable needs to withstand a high current of 150 A. The high-power ring has a much larger size. Fig. 16 also compares targeted suppression with a small magnetic ring and typical suppression with a large magnetic ring, and it is clear that targeted suppression significantly increases the power density. The parameters of the magnetic ring are shown in Table VI.

Fig. 17 shows the LF multisource EMI before and after targeted suppression. In the 400 kHz–1 MHz band, the targeted suppression strategy for the DCAUX achieves a maximum suppression of 18 dB. Besides, other frequency bands that are not dominated by DCAUX have almost no changes. The results verify the correctness of LF EMI decoupling.

C. Validation of HF Multisource EMI Decoupling

The HF multisource EMI decoupling is validated in two aspects. First, the row-vector-based identification results and the column-vector-based decoupling results are compared to mutually verify the correctness. Second, targeted suppression strategies for HF EMI are implemented for further validation.

1) Validation Based on Row and Column Vectors: Table V shows the identification results of the dominant EMI sources at several key frequencies based on the time–frequency matrix row vectors.

Fig. 18 shows the time domain waveforms of HF CE multisource EMI and decoupled single-source EMI based on the column vectors. The decoupled radiated EMI results are similar and not repeated. The decoupled time-domain EMI is also

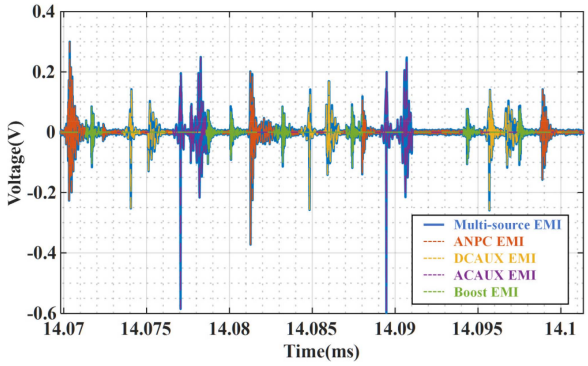

Fig. 18. Time domain waveform comparison of the multisource EMI and the decoupled single-source EMI in the HF CE band.

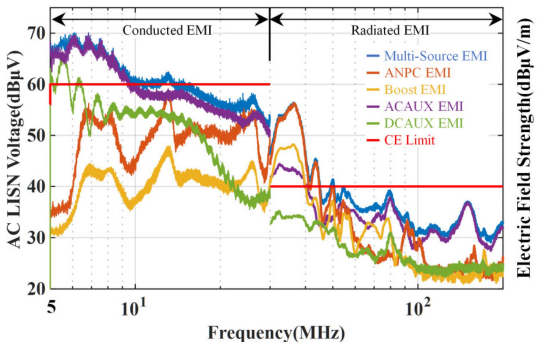

Fig. 19. QP spectrum comparison of the HF multisource EMI with decoupled single-source EMI.

detected for the QP results by a simulated EMI receiver program [27]. The HF CE and RE QP spectrums results are combined in Fig. 19. Due to the different units of the CE and RE curves, the curves are not continuous at 30 MHz.

By analyzing the magnitudes of the decoupled QP EMI, it can be seen that the results in Table V and Fig. 19 validate each other. For example, the dominant EMI source identified in Table V at 35 MHz is the ANPC and the curve with the highest amplitude at 35 MHz in Fig. 19 is also the ANPC. The other key frequencies are also mutually verified. The results validate the correctness of HF EMI decoupling.

Note that when the EMI of two sources has similar QP values, the row-vector-based identification method prioritizes ANPC as the dominant EMI source. This is because spikes of ANPC vary with the magnitude of the power sinusoidal current and have larger peaks compared to the smooth spikes of the dc/dc converters. The decoupled ANPC QP value at 13 MHz is equal to that of ACAUX in Fig. 19, and the dominant EMI source identified in Table V is ANPC. This also shows that the essence of row-vector-based dominant source identification is only peak identification, though it is much simpler. The multisource EMI decoupling method based on column vectors has the superiority of being able to perform QP/AV postprocessing.

2) Validation Based on Targeted Suppression: As shown in Fig. 19, the peak HF EMI frequency is 6 MHz for CE and 35 MHz for RE. The ACAUX and ANPC are the corresponding dominant sources that need targeted suppression.

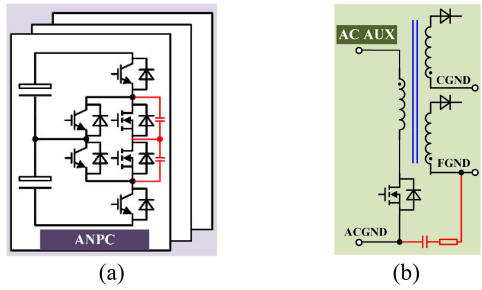

Fig. 20. Targeted suppression for HF multisource EMI. (a) Buffer circuits for ANPC. (b) *Y*-capacitors for ACAUX.

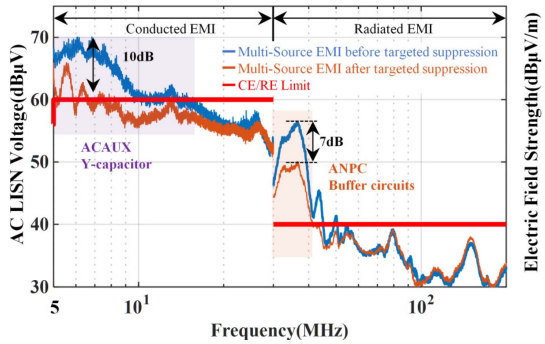

Fig. 21. QP spectrum comparison of the HF multisource EMI before and after targeted suppression.

For the HF CE EMI, a magnetic ring cannot be installed at the input of the ACAUX like DCAUX. Because the converter has no interconnect cable but only PCB traces. In this case, adding *Y*-capacitors is a good choice [32]. For the HF RE EMI, a few cancellation techniques work well in this band. Buffer circuits may be a not bad choice.

Fig. 20 illustrates the targeted suppression strategy for the ACAUX and ANPC. The *Y* capacitors are installed between the primary side ACGND and the secondary side FGND in ACAUX to suppress HF CE EMI. The damping resistors are also added to avoid resonance. The FGND of the ACAUX is the reference ground of the drive fan circuit, with a large current and more turns in the winding, generating a larger CM current. The *Y* capacitor is therefore installed to suppress EMI from FGND. The value of the *Y* capacitor and damping resistor are 4.7 nF and 1 Ω respectively, as shown in Table VI.

The operating frequency of SiC in ANPC is 20 kHz, much higher than the 50 Hz operating frequency of Si devices. The higher switching frequency generates EMI with higher amplitude, so the SiC device is the main EMI source in the ANPC and the buffer circuits should be connected in parallel to the SiC devices. Buffer circuits of 1.5 nF capacitor are installed parallel with ANPC's SiC switching devices to suppress HF RE EMI. The buffer capacitors can reduce the switching speed of the SiC devices, which significantly suppresses HF EMI [25].

Fig. 21 shows the CE and RE EMI spectra before and after the targeted suppression strategies. In the 5–10 MHz band, the targeted strategy of the *Y* capacitor for ACAUX achieves a maximum suppression of 10 dB. In the 30–40 MHz band,

the targeted strategy of the buffer circuits for ANPC achieves a maximum suppression of 7 dB. The results verify the correctness of HF EMI decoupling.

VI. Conclusion

Multisource EMI decoupling method for a 100-kW PV inverter is proposed in this article. The analysis of the LF and HF spectrum leads to two different parts of the proposed decoupling method. The LF multisource EMI is decoupled based on the discrete spectrum. The HF multisource EMI is decoupled based on the time–frequency matrix due to its continuous spectrum. Experiments on the 100 kW PV inverter are conducted to validate the proposed decoupling method. Based on the decoupled single-source EMI, targeted suppression strategies for dominant EMI sources are proposed and implemented. The suppression results validate the correctness of both the LF and HF multisource EMI decoupling methods.

The proposed decoupling method can be applied to various power electronic systems, and make the prediction and suppression more targeted.

References

[1] J. Wang, X. Liu, Y. Xun, and S. Yu, "Common mode noise reduction of three-level active neutral point clamped inverters with uncertain parasitic capacitance of photovoltaic panels," *IEEE Trans. Power Electron.*, vol. 35, no. 7, pp. 6974–6988, Jul. 2020.

[2] H. Zhang, L. Yang, S. Wang, and J. Puukko, "Common-mode EMI noise modeling and reduction with balance technique for three-level neutral point clamped topology," *IEEE Trans. Ind. Electron.*, vol. 64, no. 9, pp. 7563–7573, Sep. 2017.

[3] S. Padmanaban, M. Khalili, M. A. Nasab, M. Zand, A. G. Shamim, and B. Khan, "Determination of power transformers health index using parameters affecting the transformer's life," *IETE J. Res.*, vol. 69, no. 11, pp. 8467–8488, 2023.

[4] S. Norouzi, H. Ghoreishy, A. A. Ahmad, and F. Tahami, "Stability analysis of variable frequency control method of soft switching for boost converter with wide bandgap semiconductors," in *Proc. 14th Power Electron., Drive Syst., Technol. Conf.*, 2023, pp. 1–7, doi: 10.1109/PEDSTC57673.2023.10087093.

[5] *Photovoltaic Power Generating Systems — EMC Requirements and Test Methods for Power Conversion Equipment*, Standard IEC 62920, International Electrotechnical Commission, Geneva, Switzerland, 2021.

[6] P. Zhou, X. Pei, Q. Chen, Y. Zhang, and H. Fan, "EMI behavioral model based CM noise prediction method for DC power system considering multi-noise coupling," *IEEE Trans. Power Electron.*, vol. 38, no. 4, pp. 4658–4667, Apr. 2023.

[7] P. Zhou, X. Pei, K. Zhang, and Y. Shan, "Improved EMI behavioral modeling method of three-phase inverter based on the noise-source phase alignment," *IEEE Trans. Power Electron.*, vol. 37, no. 8, pp. 9333–9344, Aug. 2022.

[8] J. Wang et al., "Co-reduction of common mode noise and loop current of three-level active neutral point clamped inverters," *IEEE J. Emerg. Sel. Topics Power Electron.*, vol. 9, no. 1, pp. 1088–1103, Feb. 2021.

[9] Z. Ma, Y. Li, S. Wang, H. Sheng, and S. Lakshmikanthan, "Investigation and reduction of EMI noise due to the reverse recovery currents of 50/60 Hz diode rectifiers," *IEEE J. Emerg. Sel. Topics Ind. Electron.*, vol. 3, no. 3, pp. 594–603, Jul. 2022.

[10] D. Nemashkalo, N. Moonen, and F. Leferink, "Multi-channel time-domain EMI evaluation of dominant mode interference for optimized filter design in three-phase systems," in *Proc. IEEE Int. Symp. Electromagn. Compat. Signal/Power Integrity*, 2020, pp. 205–208.

[11] W. Shen, F. Wang, D. Boroyevich, and Y. Liu, "Definition and acquisition of CM and DM EMI noise for general-purpose adjustable speed motor drives," in *Proc. IEEE 35th Annu. Power Electron. Specialists Conf.*, 2004, vol. 2, pp. 1028–1033.

[12] X. Gao and D. Su, "Suppression of a certain vehicle electrical field and magnetic field radiation resonance point," *IEEE Trans. Veh. Technol.*, vol. 67, no. 1, pp. 226–234, Jan. 2018.

[13] L. Yang, H. Zhao, S. Wang, and Y. Zhi, "Common-mode EMI noise analysis and reduction for AC–DC–AC systems with paralleled power modules," *IEEE Trans. Power. Electron.*, vol. 35, no. 7, pp. 6989–7000, Jul. 2020.

[14] U. Paoletti, "Scalar matching indexes for broadband EM noise source determination with one-port measurements," *IEEE Trans. Electromagn. Compat.*, vol. 64, no. 3, pp. 613–622, Jun. 2022.

[15] U. Paoletti, "Modulation frequency analysis for EMC," *IEEE Electromagn. Compat. Mag.*, vol. 12, no. 3, pp. 79–85, 3rd Quarter 2023.

[16] U. Paoletti, "Single-channel blind source separation for periodic electromagnetic switching noise," *IEEE Trans. Electromagn. Compat.*, vol. 65, no. 5, pp. 1300–1308, Oct. 2023.

[17] L. Xiaozhu, H. Bo, W. Qi, and S. Donglin, "A novel blind source separation algorithm for electromagnetic interference sources identification," in *Proc. Int. Appl. Comput. Electromagn. Soc. Symp.*, 2021, pp. 1–2.

[18] F. Zhang, W. Wang, D. Zhang, A. Chen, and D. Su, "Radiation emitter classification and identification approach based on radiation emission components," *Appl. Sci.*, vol. 12, no. 16, 2022, Art. no. 8193, doi: 10.3390/app12168193.

[19] D. Su, S. Xie, A. Chen, X. Shang, K. Zhu, and H. Xu, "Basic emission waveform theory: A novel interpretation and source identification method for electromagnetic emission of complex systems," *IEEE Trans. Electromagn. Compat.*, vol. 60, no. 5, pp. 1330–1339, Oct. 2018, doi: 10.1109/TEMC.2017.2771454.

[20] M. A. Azpúrua, M. Pous, and F. Silva, "Decomposition of electromagnetic interferences in the time-domain," *IEEE Trans. Electromagn. Compat.*, vol. 58, no. 2, pp. 385–392, Apr. 2016.

[21] C. Xiao and T. Zhao, "Identification method of EMI sources based on measured single-channel signal and its application in aviation secondary power source design," *IEEE Trans. Electromagn. Compat.*, vol. 59, no. 2, pp. 439–446, Apr. 2017, doi: 10.1109/TEMC.2016.2612704.

[22] P. Li, Z. Zhou, and M. Sheng, "Identification of electromagnetic interferences based on adaptive sparsest time — Frequency analysis," in *Proc. IEEE Int. Symp. Electromagn. Compat. IEEE Asia-Pacific Symp. Electromagn. Compat.*, 2018, pp. 761–765, doi: 10.1109/ISEMC.2018.8393884.

[23] F. Vargas, D. Borba, J. D. Benfica, and R. T. Syed, "Artificial neural network accelerator for classification of in-field conducted noise in integrated circuits' DC power lines," in *Proc. IEEE 29th Int. Symp. -Line Testing Robust System Des.*, 2023, pp. 1–6.

[24] X. C. Wei, Y. F. Shu, Z. K. Hu, Y. H. Zhong, and Y. W. Wang, "A summary of artificial neural networks on electromagnetic interference diagnosis," in *Proc. Int. Conf. Microw. Millimeter Wave Technol.*, 2019, pp. 1–3, doi: 10.1109/ICMMT45702.2019.8992910.

[25] D. Han, S. Li, Y. Wu, W. Choi, and B. Sarlioglu, "Comparative analysis on conducted CM EMI emission of motor drives: WBG versus si devices," *IEEE Trans. Ind. Electron.*, vol. 64, no. 10, pp. 8353–8363, Oct. 2017.

[26] J. Chen, D. Jiang, W. Sun, Z. Shen, and Y. Zhang, "A family of spread-spectrum modulation schemes based on distribution characteristics to reduce conducted EMI for power electronics converters," *IEEE Trans. Ind. Appl.*, vol. 56, no. 5, pp. 5142–5157, Sep./Oct. 2020.

[27] Y. Yu, X. Pei, Q. Chen, P. Zhou, and D. Zhao, "A fast method for predicting the quasi-peak radiated EMI spectrum of power converters," in *Proc. IEEE Energy Convers. Congr. Expo.*, 2023, pp. 3415–3421.

[28] Y. Yu, P. Zhou, X. Pei, D. Zhao, Q. Chen, and Y. Zhang, "Modeling and analysis of multi-source spectrum in PV inverter considering EMI accumulation effect," in *Proc. IEEE 2nd Int. Power Electron. Appl. Symp.*, 2023, pp. 1750–1756.

[29] E. M. Stein and R. Shakarchi, *Fourier Analysis: An Introduction*, vol. 1. Princeton, NJ, USA: Princeton Univ. Press, 2011.

[30] R. Polikar, "The wavelet tutorial," Jun. 1995. [Online]. Available: https://users.rowan.edu/∼polikar/WTtutorial.html

[31] P. M. Baggenstoss, "On the equivalence of hanning-weighted and overlapped analysis windows using different window sizes," *IEEE Signal Process. Lett.*, vol. 19, no. 1, pp. 27–30, Jan. 2012.

[32] H. Zhang, S. Wang, Y. Li, Q. Wang, and D. Fu, "Two-capacitor transformer winding capacitance models for common-mode EMI noise analysis in isolated DC–DC converters," *IEEE Trans. Power. Electron.*, vol. 32, no. 11, pp. 8458–8469, Nov. 2017.

[33] D. Menzi, D. Bortis, and J. W. Kolar, "EMI filter design for a three-phase buck–boost Y-inverter VSD with unshielded motor cables considering IEC 61800-3 conducted and radiated emission limits," *IEEE Trans. Power Electron.*, vol. 36, no. 11, pp. 12919–12937, Nov. 2021, doi: 10.1109/TPEL.2021.3075785.